2019

Luminescent calcium carbonate micro 'bow ties'

Fearghal C. Donnelly

Finn Purcell-Milton

Peter W. Dunne

See next page for additional authors

Authors

Fearghal C. Donnelly, Finn Purcell-Milton, Peter W. Dunne, Aleksandra Rulikowska, Victor Alguacil, and Yurii K. Gun'ko

Luminescent calcium carbonate micro 'bow ties'

Fearghal C. Donnelly[a,b], Finn Purcell-Milton[a,b], Peter W. Dunne[a], Aleksandra Rulikowska[c], Victor Alguacil[d], Yurii K. Gun'ko[a,b,*]

[a] *School of Chemistry, Trinity College Dublin, Dublin 2, Ireland*
[b] *BEACON, Bioeconomy Research Centre, University College Dublin, Dublin 4, Ireland*
[c] *ESHI, Technological University Dublin, Grangegorman, Dublin 7, Ireland*
[d] *Complutense University of Madrid, Av. Séneca, 2, 28040, Madrid, Spain*

A B S T R A C T

Calcium carbonate ($CaCO_3$) is a ubiquitous material which has been studied for centuries due to its integral nature across various fields and its vast range of applications. Here we report, for the first time, a low temperature dry ice carbonation method for the production of unique rare earth-doped calcium carbonate 'bow ties'. $CaCO_3$ exhibits retrograde solubility, an interesting property in which its solubility increases with decreasing temperature. In this synthesis, dry ice acts not only as a CO_2 source, but as a coolant, increasing the solubility of $CaCO_3$ and CO_2 and allowing specific growth to occur. The incorporation of trivalent lanthanide ions Eu^{3+} and Tb^{3+} into the $CaCO_3$ synthesis results in the formation of these unique luminescent calcite 'bow tie' microstructures which cannot be produced using either standard gaseous CO_2 carbonation, or chemical precipitation methods. This new method and materials might find potential applications including, but not limited to, radionuclide sequestration, imaging and photonics.

1. Introduction

Calcium carbonate is a highly important material with numerous applications in many fields - from a filler material in plastics and paints [1], as the material of choice for high gloss paper, as well as its use in biomedicine where it displays excellent biocompatibility and finds uses in antacids, calcium supplementation, as well as drug delivery [2,3]. Calcium carbonate exists in three anhydrous polymorphs: calcite, aragonite, and vaterite; with a further three hydrated forms: amorphous calcium carbonate (ACC), ikaite, and monohydrocalcite [4]. Calcite, the most stable and commonly observed polymorph, belongs to the hexagonal crystal system and typically presents as rhombohedral crystals which form preferentially at room temperature. Aragonite, the second most stable form, is in the orthorhombic system and usually adopts acicular, or needle-like morphologies. Vaterite, the metastable form, belongs to the hexagonal system and is most commonly found as polycrystalline microspheres.

In addition to its vast number of industrial applications, calcium carbonate is also of enormous importance in the natural world as a major biomineral [5] and a significant global CO_2 sink [6]. During biomineralisation, dissolved Ca^{2+} and CO_3^{2-} react to form calcium carbonate with precise and elegant structural and morphological

control driven by underlying biological structure-directing agents and processes. This results in shapes which act as the major structural support in molluscs and echinoderms, as well as thin $CaCO_3$ layers which form corals. As the various roles played by calcium carbonate in nature are so heavily dependent on the phase and morphology adopted, achieving the same level of control *in vitro* has long been an area of considerable research [7].

A further advantage of calcium carbonate, and calcite in particular, is its capacity to adsorb and incorporate other ions. This has potential implications for the remediation and sequestration of hazardous metals and radionuclides from both natural and anthropogenic sources. The capacity of calcite to act as a radionuclide trap has previously been examined using trivalent lanthanide ions as non-radioactive analogues. These studies have shown that the lanthanide ions have a high partition coefficient with calcite, with various lanthanide ions readily incorporated into the calcite lattice, though the precise mechanism of incorporation remains the subject of some debate [8,9]. The use of rare earth dopants in $CaCO_3$ opens up unique opportunities to produce new biocompatible, luminescent materials, which may offer many advantages over other sources of luminescence such as quantum dots [10] or organic dyes [11]. These advantages include high stability and biocompatibility, coupled with narrow emission bands and large Stokes
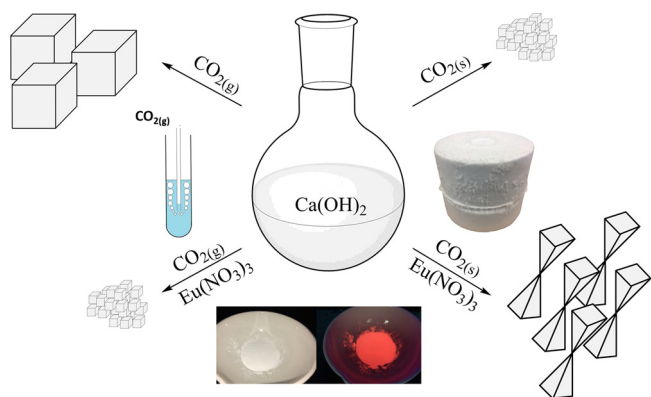

Scheme 1. Synthetic scheme illustrating the effect of both the method of CO_2 introduction as well as the presence of lanthanide dopants.

shifts typical of the lanthanides.

Despite its long history, the controllable synthesis of calcium carbonate based nano- and microstructures still remains the focus of intense research as it presents many challenges, with its various applications dependent on the exact morphology and polymorph produced [12]. The two most common synthetic techniques are precipitation of Ca^{2+} and CO_3^{2-} containing salts, or carbonation using gaseous CO_2 – the industrially preferred approach. Recently, we have reported a new method of preparing $CaCO_3$ nanoparticles using dry ice, or solid CO_2 carbonation [13]. In this method, dry ice acts as both a CO_2 source and

a coolant, exploiting the retrograde solubility of $CaCO_3$ which offers greater control over the phase, size and morphology of the calcium carbonate product obtained. Here we apply the new dry ice carbonation method to the synthesis of unique lanthanide-doped calcite microstructures.

2. Results and discussion

The synthesis of the lanthanide-doped calcium carbonate (Scheme 1) was performed by dissolving CaO in Millipore water with appropriate amounts of the lanthanide nitrate salt (($Eu(NO_3)_3$, $Tb(NO_3)_3$ or $Ce(NO_3)_3$), followed by the sequential addition of dry ice (solid CO_2) until a pH of 7 was reached. The solid products were isolated by centrifugation and washed with water and ethanol prior to drying at 80 °C for 24 h. Samples were characterised by X-ray powder diffraction (XRD), scanning electron microscopy (SEM), energy dispersive X-ray analysis (EDX), steady state photoluminescence spectroscopy, time-dependent photoluminescent decay spectroscopy and inductively coupled plasma mass spectrometry (ICP-MS). ICP-MS were broadly in line with that expected (see table S1, supporting information).

Scanning electron microscopy (SEM) images showed the formation of unique structures of $CaCO_3$ (see Fig. 1), which appear to have a central nucleation point, which grows through acicular-like structures to form an anisotropic material, the morphology of which we have termed as 'bow tie'. The structures formed an average length of $11.1 \pm 2.7\,\mu m$ when measured end to end (see histogram, Figure S1 (A)). The 'bow ties' formed also exhibit a readily visible porous

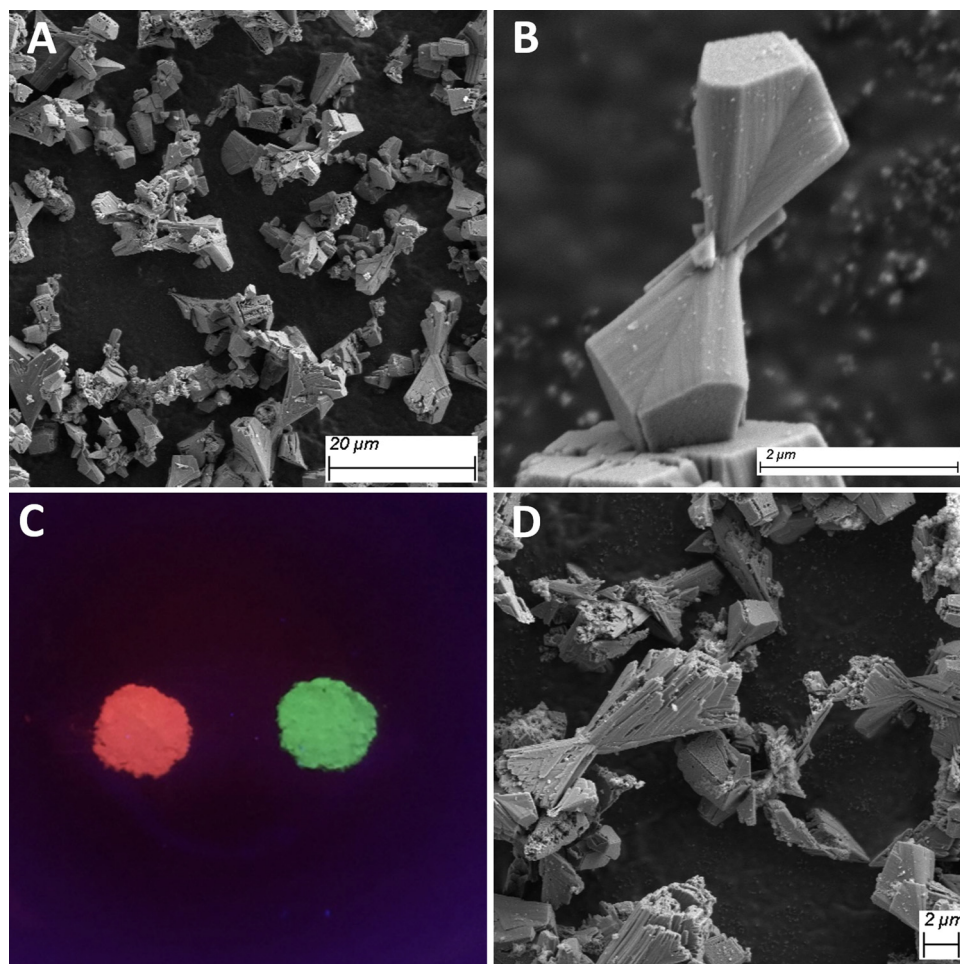**Fig. 1.** (A) and (B) SEM images of 3.4 mol % Eu^{3+} doped $CaCO_3$ 'bow ties' (C) photos of Eu^{3+} (left) and Tb^{3+} (right) doped $CaCO_3$ samples under UV light and (D) SEM image of 2.5 mol % Tb^{3+} doped $CaCO_3$ 'bow ties'.
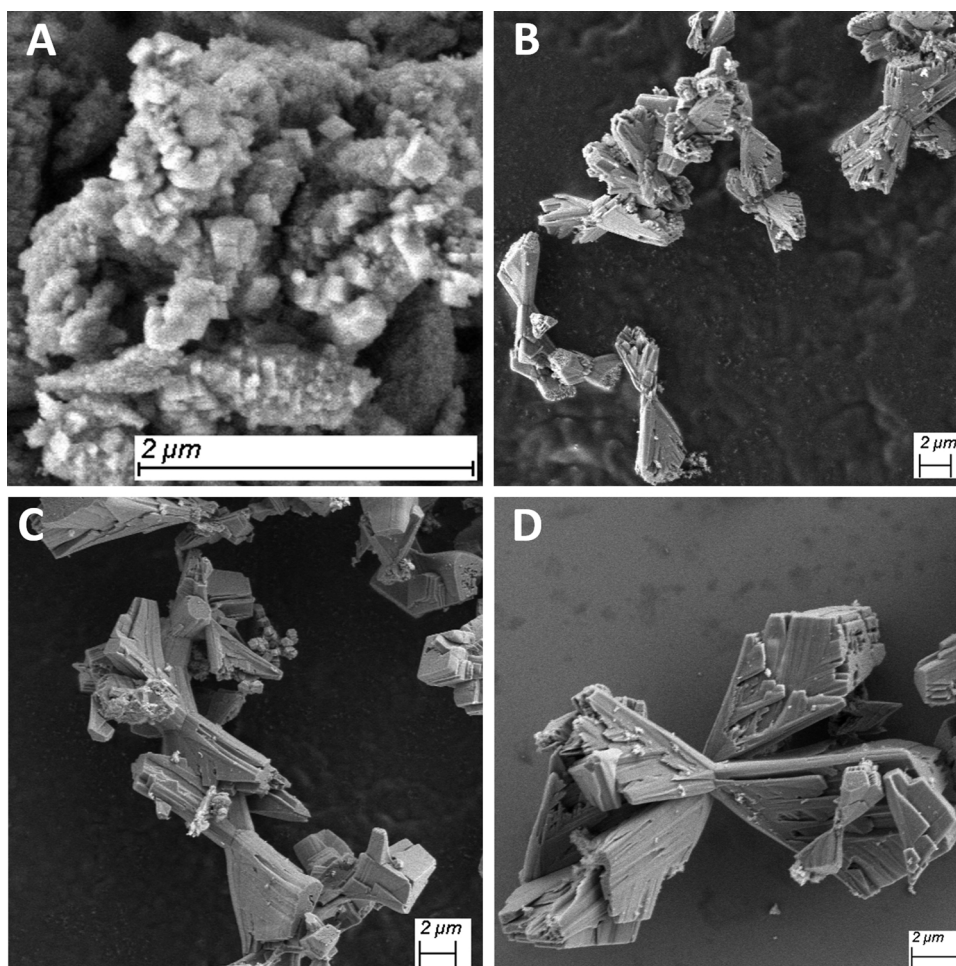
Fig. 2. SEM images of CaCO$_3$ obtained at Eu^{3+} doping levels of (A) 0.5 (B) 1.68 (C) 2.5 and (D) 3.4 mol %.

morphology at their ends (see Figure S2). This porosity adds a further layer of interest to these materials which potentially enables their use for encapsulation. Interestingly, we have found that without the addition of Eu^{3+}, no 'bow tie' structures were present, instead forming small calcite nanoparticles which is typical of dry ice carbonation [13]. It was revealed that the 'bow tie' morphology only appears at concentrations of Eu^{3+} of 1.68 mol % and above (see Fig. 2). This implies that there must be a sufficient concentration of a lanthanide dopant to induce anisotropy and therefore invoke the 'bow tie' formation mechanism in the calcite structures. In addition, the gross 'bow tie' morphology is retained on further increasing the Eu^{3+} concentration with only minor changes in morphology observed. The same behaviour was found to occur from Tb^{3+} doping, with three concentrations examined in detail, giving the onset of the 'bow tie' type morphology with concentrations at or above 1.68 mol %, and showing an average size of 10.3 ± 2.9 μm (Figure S1 (B)), with SEM images given in supporting information (Figure S3). A series of experiments using conventional gaseous CO$_2$ bubbling and chemical precipitation methods were also carried out with the same materials and concentration range, however these experiments did not result in any similar 'bow tie' microstructures (see Fig. 3).

This is the first known report of calcite 'bow ties' with no similar structures being reported for CaCO$_3$, either doped or undoped. The fact that these structures were only encountered using the dry ice method in the presence of lanthanide ions (Fig. 3 (B)) suggests that the lanthanides must play a significant role (dry ice carbonation without the presence of lanthanides results in the formation of rhombohedral nanoparticles (Fig. 3 (D))). There exists both a size and charge disparity between the

divalent calcium and trivalent lanthanide cations, with Ca^{2+} having an ionic radius of 114 pm, while Eu^{3+} and Tb^{3+} have radii of 108.7 and 106.3 pm, respectively [14]. The influence of the size disparity was investigated by substituting Ce(NO$_3$)$_3$ (which has an ionic radius similar to Ca^{2+} at 115 pm) for Eu(NO$_3$)$_3$ and carrying out otherwise identical reactions at Ce^{3+} levels of 0.5 to 3.4 mol % (see supporting information, Table S3). All Ce^{3+} doped samples were also identified by XRD as phase pure calcite; however the 'bow tie' morphologies were not observed, with large rhombohedral microparticles obtained in their place (see Fig. 3 (C)) suggesting that the ionic radius of the Ce^{3+} dopant was not sufficiently different to induce 'bow tie' formation. Additional syntheses were performed using EuCl$_3$ to explore the effect of the nitrate counter ions, as these have previously been identified as having a significant influence on lanthanide uptake into calcite. It was found that the products obtained from dry ice carbonation with EuCl$_3$ also yielded the 'bow tie' structures (see Figure S4). It can thus be concluded that the lanthanide ions are responsible for the observed morphology, with the charge disparity likely causing the increased particle size, relative to the undoped samples, while the difference in ionic radii between Eu^{3+} or Tb^{3+} and Ca^{2+} induces the formation of the unusual 'bow tie' structures. While these 'bow ties' are absolutely unique for CaCO$_3$, similar morphologies have previously been observed in the crystallisation of BaSO$_4$ at the air-water interface in the presence of organic surfactant monolayers. These studies have attributed the unusual BaSO$_4$ 'bow tie' morphologies obtained to the adsorption of the surfactant species to specific facets, which could be further influenced by varying the dielectric constant of the interface [15,16]. This enables us to suggest that at higher lanthanide concentrations a surface-bound lanthanide
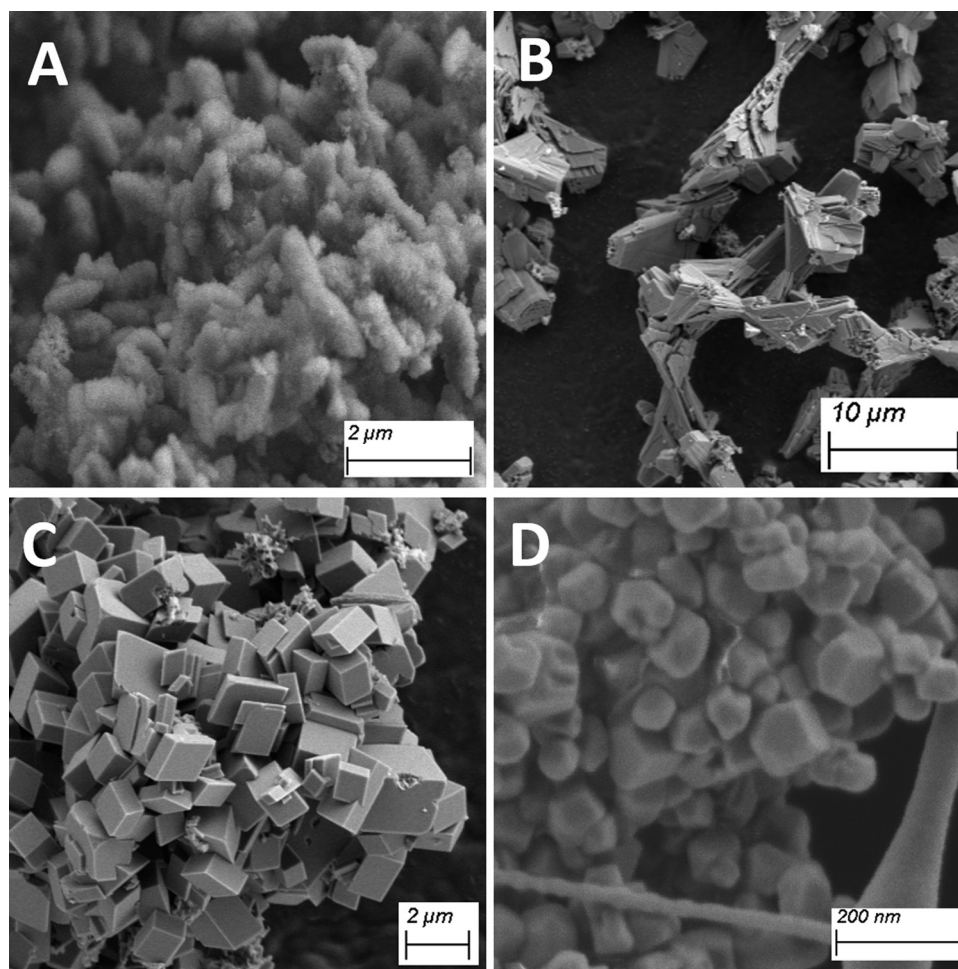
Fig. 3. SEM images of $CaCO_3$ produced with 3.4 mol % Eu^{3+} via (A) CO_2 bubbling and (B) dry ice carbonation. $CaCO_3$ produced with (C) 3.4 mol % Ce^{3+} and (D) without lanthanide present.
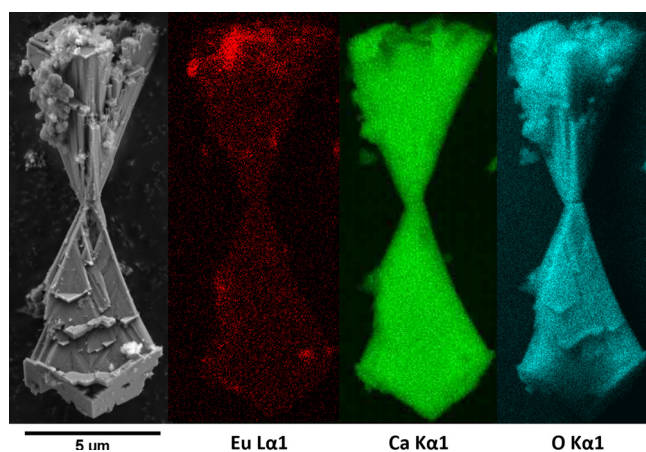

Fig. 4. Images and EDX analysis of the 'bow tie' structures showing their elemental composition with Eu (Red), Ca (green) and O (blue).

carbonate species is involved in directing the growth of the 'bow ties'.

In addition to the clear impact of the dopant ions, the use of the dry ice carbonation method [13] is also found to be a key requirement in forming these new structures. By performing the carbonation step using the conventional CO_2 bubbling method, only rhombohedral nanoparticles were obtained, even in the presence of 3.4 mol % Eu^{3+} (Fig. 3 (A)). The fact that the 'bow tie' morphology is only obtained from the dry ice carbonation method is attributed to the cooling effect of the dry

ice. Due to the retrograde solubility of $CaCO_3$ [17] and CO_2 [18], cooling the system increases the solubility of both, thus allowing more significant growth to occur with the influence of the lanthanide ions leading to the 'bow tie' morphology. EDX analysis showed that the lanthanides are evenly distributed throughout the structures, as shown in Fig. 4.

The XRD patterns (Fig. 5 (A) and (B)) of all samples confirm that only phase pure calcite is obtained, regardless of dopant or dopant concentration. While no other phases are observed, Rietveld refinement shows some significant changes in unit cell parameters (see Figure S5 and Table S4, supporting information). Upon the inclusion of 0.5 mol % Eu^{3+} in the synthesis, the unit cell volume increases from 367.66 Å^3 for the undoped calcite, to 369.30 Å^3 for that prepared by this procedure. As the dopant level is further increased to 1.68 mol % and above, the cell volume returns to its initial value (Fig. 5 (C)). This may indicate that at lower dopant levels the Eu^{3+} is incorporated into the calcite lattice, while at higher concentrations a surface doping mechanism may predominate.

The excitation photoluminescence spectra (PLEx) and the emission photoluminescence spectra (PLEm) of Eu^{3+} doped $CaCO_3$ showed the characteristic spectrum of Eu^{3+} as illustrated by the 1.68 mol % Eu^{3+} doping level shown in Fig. 6 (A) (spectra for all other doping levels can be found in supporting information, Figure S6). PLEm was measured from 560 nm to 720 nm using an excitation wavelength of 393 nm corresponding to the $^7F_0$–$^5L_6$ transition and 270 nm which is related to the absorption energy of the O^{2-} / Eu^{3+} charge transfer band (CTB) [19]. PLEx was measured from 230 nm to 500 nm using the 614 nm
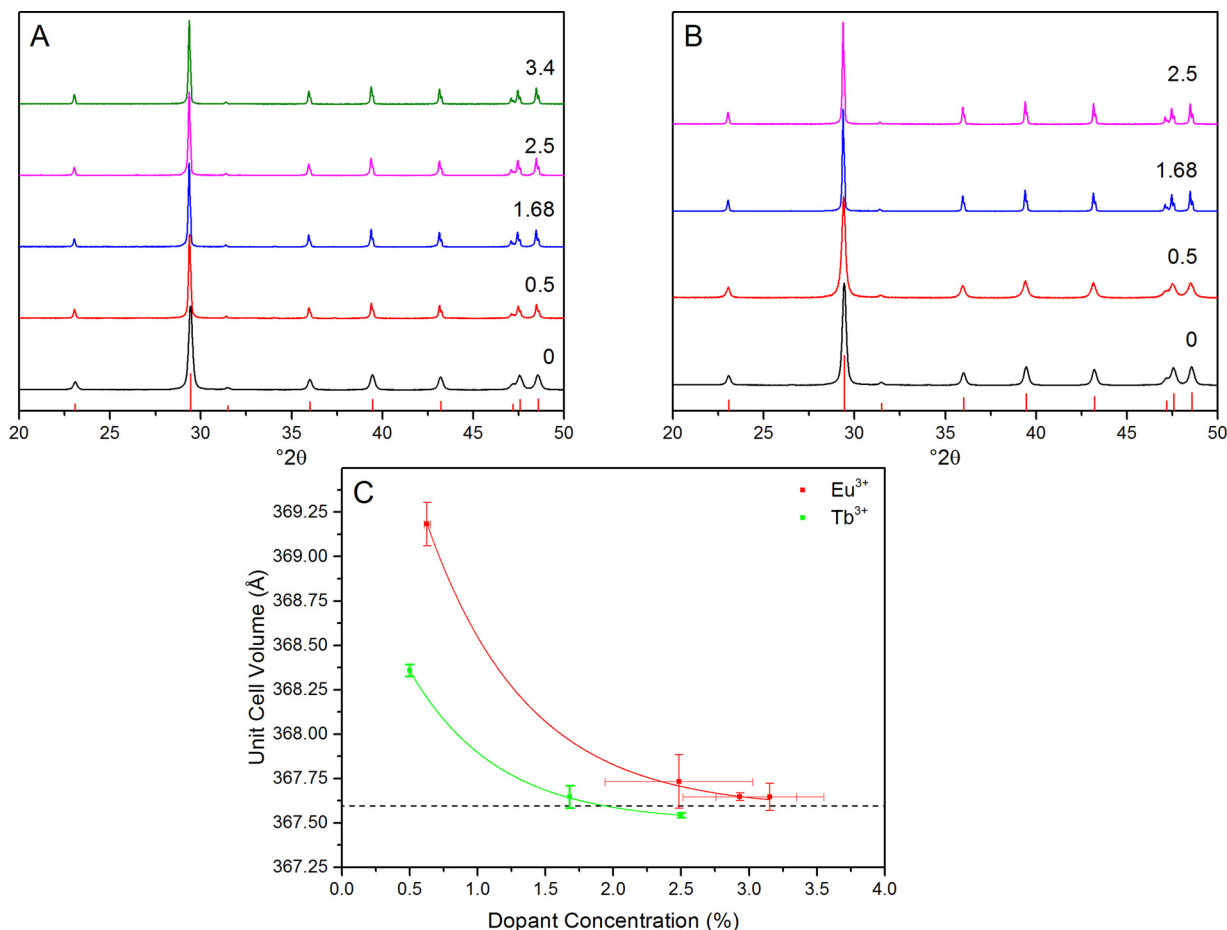
Fig. 5. (A and B) XRD patterns of the various doping levels of CaCO$_3$ doped with Eu^{3+} and Tb^{3+}, respectively (the characteristic pattern of calcite is illustrated as red lines) (C) cell volume (Å^3) vs dopant concentration (%) determined by Rietveld refinement and ICP-MS, respectively.
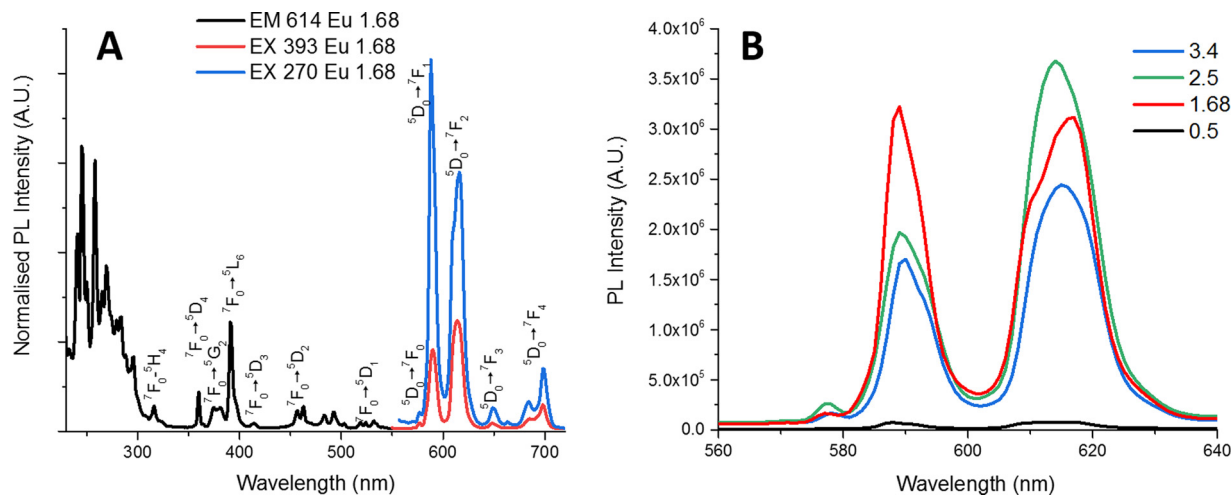

Fig. 6. (A) Emission and excitation photoluminescence spectra of 1.68 mol % Eu^{3+} doped CaCO$_3$ and (B) comparative emission intensities of the two most intense transitions ($^5D_0$–$^7F_1$, $^5D_0$–$^7F_2$) for the various doping levels.

emission peak. The excitation spectra contain a group of sharp peaks in the longer wavelength region, which can be ascribed to the f–f transitions within the 4f^6 configuration of Eu^{3+} ions. Upon excitation at 393 nm, the emission spectrum is composed of a group of lines peaking at 579, 590, 613, 650 and 699 nm. They correspond to the $^5D_0$–^7F_J (J = 0, 1, 2, 3, 4) transition of the Eu^{3+} ions, respectively. The strongest peak is located at 613 nm, which is the characteristic peak of Eu^{3+} ions. The excitation intensity changes between 270 and 393 nm,

whereby the intensity of luminescence is far higher at 270 nm for lower dopant concentrations, with the emission at ex. 393 nm steadily increasing as the dopant concentration tends towards 3.4 mol %.

In addition, it is interesting to note that the $^5D_0$–$^7F_2$ transition is a forced (induced) electric dipole type of transition [20], the intensity of which depends strongly on the symmetry of the Eu^{3+} environment. However, $^5D_0$–$^7F_1$ is magnetic-dipole allowed and is independent of local symmetry [21]. Therefore the ratio between the $^5D_0$–$^7F_1$ and
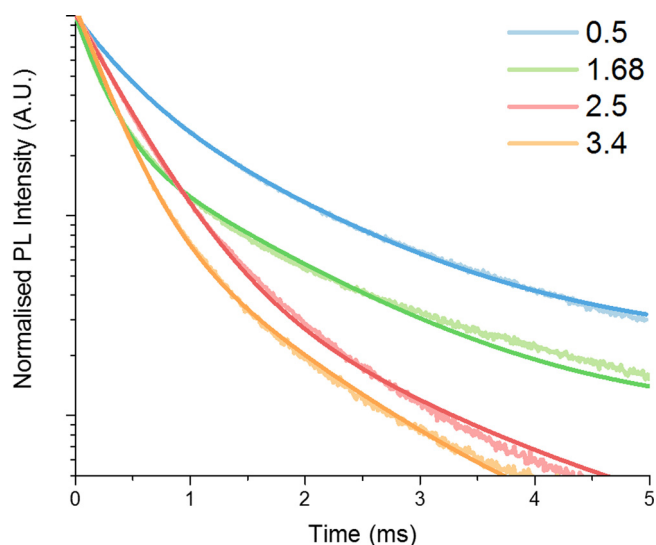
Fig. 7. Photoluminescent decay curves of CaCO$_3$ doped with 0.5, 1.68, 2.5, and 3.4 mol % Eu^{3+} using a 393 nm excitation.

$^5D_0$–$^7F_2$ intensity peaks is termed the asymmetry ratio (R) and has been previously reported in literature [19] to correspond to the site asymmetry of the Eu^{3+} ion and can be evaluated for each doping level from the ratio of the areas of the peaks between the $^5D_0$–$^7F_2$ electric dipole transition and the $^5D_0$–$^7F_1$ magnetic dipole transition using the equation shown in eqn. 1 [22].

$$R = I(^5D_0-^7F_1)/I(^5D_0-^7F_2) \tag{1}$$

This information is presented in Table S5 and indicates that a minor increase in asymmetry occurs with increasing Eu^{3+} levels.

A comparison of the emission intensities (ex. 270 nm) between different Eu^{3+} doping levels of the two most intense transitions ($^5D_0$–$^7F_1$, $^5D_0$–$^7F_2$) is shown in Fig. 6 (B). Two distinct trends are observed: a strong increase in emission intensity when comparing 0.5 to 1.68 mol % Eu^{3+}, and a decrease in emission intensity above 2.5 mol % Eu^{3+} (the percentage change relative to intensity is given in supporting information, Table S6). Firstly, the dramatic increase in emission intensity is proposed to be strongly correlated with the new morphology which evolves as Eu^{3+} doping level increases, forming the larger 'bow tie' structures. In this case, the surface area to volume strongly decreases as a result of the large increase in crystallite size, therefore reducing surface quenching of the Eu^{3+} centres [23]. The decrease in

Eu^{3+} emission found at doping levels above 2.5 mol % has previously been reported as concentration quenching [24,25] and has been explained by the occurrence of Ln-O-Ln interactions in the material in a range of host matrixes [22,26] including distance-dependent resonance energy transfer and cross-relaxation transmission [27]. Secondly, it has been proposed that Eu^{3+} incorporation into the Ca based lattices, replaces the Ca^{2+} in the lattice causing a charge disparity – hence as doping increases the lattice vacancies will increase too [22,26]. These vacancies have been shown to cause quenching by providing an alternative de-excitation route from the excited Eu^{3+} ions.

A further investigation of the resulting phosphorescent lifetimes was carried out with the resulting decay graphs illustrated in Fig. 7 (further information can be found in Tables S7 and S8, supporting information). Samples were measured from the 614 nm emission peak, while exciting at 393 nm. This data was fitted using a bi-exponential decay, giving an average time (τ_{avg}) ranging from 0.4 to 1 ms (Table S7). The reason for bi-exponential decay is due to the Eu^{3+} dopant being found in the matrix in two distinct environments, which therefore gives rise to two exponential decay times – a shorter time in the range of 0.2 -0.4 ms and a longer time of 1.0–1.5 ms. This corresponds well to reported bi-exponential fits of Eu^{3+} doped CaCO$_3$ samples in literature, explained via the deduction that Eu^{3+} is occupying two different sites [23,24,27]. Firstly the longer lifetime (slow decay, τ_2) are assigned to Eu^{3+} occupying the centrosymmetric site of the lattice, replacing Ca^{2+} while the second is due to some Eu^{3+} ions being located at low-symmetry sites and/or at non-centrosymmetric sites, formed due to lattice defects such as distortion in grain boundary and/or surface/subsurface defects gving the second shorter lifetime (fast decay, τ_1) [23]. It is known that, even with low dopant concentration, a high local concentration of Eu^{3+} ions facilitates non-radiative decay pathways, due to Eu–Eu ion interactions, leading to a shortening in lifetimes [23]. A trend was also found of decreasing τ_{avg} with increasing Eu^{3+} emission, due to the increase in contribution of τ_1 relative to τ_2 with increasing Eu^{3+} concentrations, meaning the shorter decay lifetime makes a larger contribution to the overall decay. Again, this is to be expected if the shorter lifetime is due to Eu-Eu interactions, or due to increase in crystal defect quenching sites due to Ca^{2+} vacancy production as discussed previously.

The luminescence of Tb^{3+} doped CaCO$_3$ 'bow ties' also showed the same distinctive spectra as reported in literature [28,29]. The excitation photoluminescence spectra and the emission photoluminescence spectra for 1.68 mol % Tb^{3+} are presented in Fig. 8 (A) (with 0.5 and 2.5 mol % included in supporting information, Figure S7). PLEm was measured from 450 nm to 700 nm using an excitation of 226 nm while PLEx was measured from 200 to 475 nm using the 547 nm emission peak. The excitation spectra contain a group of sharp lines in the longer
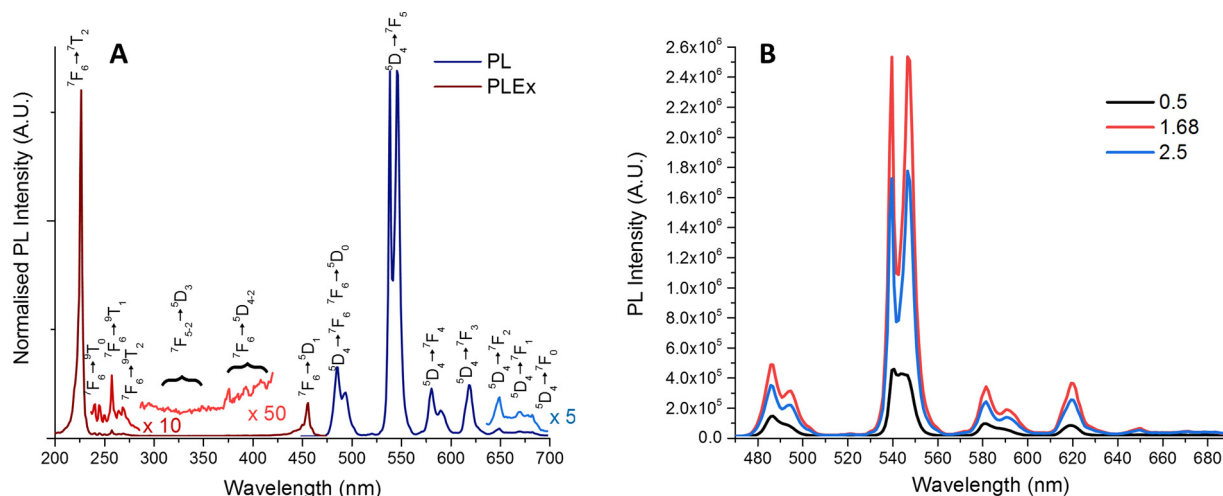

Fig. 8. (A) 1.68 mol % Tb^{3+} doped CaCO$_3$ excitation and emission spectra and (B) comparative spectra of PL emission intensities for the three dopant concentrations.

wavelength region, which can be ascribed to the f–f transitions within the $4f^8$ configuration of Tb^{3+} ions. Upon excitation at 226 nm, the emission spectrum is composed of a group of sharp lines presenting as split peaks at 486 and 495, 540 and 547, 582 and single peaks at 591, 620, 650, 672, and 684. These peaks correspond to the $^5D_4-^7F_J$ (J = 0, 1, 2, 3, 4, 5, 6) transition of the Tb^{3+} ions, respectively [30–32]. The strongest peak is located at 540 and 547 nm, which is the characteristic peak of Tb^{3+} ions. A comparison of the PL intensity of three Tb^{3+} doped samples produced (Fig. 8 (B)) shows a large increase from 0.5 to 1.68 mol % Tb^{3+}, after which a decrease in intensity is observed, albeit to a level higher than 0.5 mol % Tb^{3+}. Therefore, the Tb^{3+} doped samples show a similar trend to the Eu^{3+} doped samples, in which an increase in PL occurs when transitioning from the nanoparticle structure to the much larger 'bow tie' microstructures, after which as the Tb^{3+} concentration increases, a decrease in PL is observed due to self-quenching effects of the lanthanides. In addition, the PL decay of the 1.68 mol % doped sample (supporting information, Figure S8 and Table S9) was measured showing an average lifetime of 10.31 ± 0.04 ms which is in line with reported results in literature [33].

3. Conclusions

In summary, for the first time we have successfully synthesised luminescent anisotropic lanthanide doped calcium carbonate microstructures with a novel 'bow tie' morphology. The luminescent properties compare favourably with those previously reported for doped $CaCO_3$ based materials. An in-depth study of the effect of various dopant concentrations has also been carried out using XRD which correlates well with the luminescence results. Both studies show that at 0.5 mol % of Eu^{3+} or Tb^{3+} there is a minimal luminescence intensity corresponding with the lack of 'bow ties'. Above this point this unique 'bow tie' morphology is obtained with an associated increase in luminescence until reaching a maximum at 2.5 mol % for Eu^{3+} and 1.68 mol % for Tb^{3+} doping, above which it is reduced. This trend in luminescence most likely arises from the order of magnitude increase in size of the 'bow tie' microstructures which prevents any concentration quenching until relatively high dopant concentrations are achieved.

The actual origin of the 'bow tie' morphology is determined to occur due to a combination of lanthanide dopants which possess a size and charge disparity with the Ca^{2+} ion that they are substituting in conjunction with the dry ice carbonation method, which increases the solubility of $CaCO_3$ and CO_2 thus allowing specific growth to occur. Experiments carried out using Ce^{3+} as a dopant (with a markedly similar ionic radius to Ca^{2+}) showed no evidence of this unusual morphology, regardless of concentration. This, when considered alongside the observation that 2+ ion dopants also fail to produce 'bow ties', illustrates that they likely result due to a combination of size and charge disparity. In addtion, the importance of the dry ice carbonation method is evidenced by the absence of 'bow ties' when using gaseous CO_2 bubbling. The 'bow tie' morphology can also be conclusively linked to the presense of lanthanides and not, in fact, the counterions due to the same 'bow tie' products of the control synthesis while using $EuCl_3$ in place of $Eu(NO_3)_3$.

Overall, we believe that this work has particular importance in addressing the issue of retrograde solubility when synthesising novel $CaCO_3$ based materials, as well as the development of new materials with potential applications in a range of fields including rare earth chemistry, biological imaging and photonics.

4. Materials and methods

Experimental Procedure: 0.7 g of CaO along with varying quantities of $Eu(NO_3)_3.6H_2O$, $Tb(NO_3)_3.5H_2O$ or $Ce(NO_3)_3.6H_2O$ (see Tables S1, S2 and S3, respectively in the supporting information) were added to 25 ml of H_2O and allowed to stir for 15 min to ensure complete conversion to $Ca(OH)_2$. Subsequently, portions of a dry ice pellet (500 g) were added

sequentially. The pH was then measured to determine reaction completion (pH 7). The product was separated by centrifugation at 3000 rpm and washed with H_2O and C_2H_5OH before drying at 80 °C for 24 h.

Materials: Calcium oxide (reagent grade) was purchased from Alfa Aesar. $Eu(NO_3)_3.6H_2O$ (99.9%-Eu) was purchased from STREM chemicals while $Tb(NO_3)_3.5H_2O$ (99.9% trace metals basis), $EuCl_3.6H_2O$ (99.9% trace metals basis), and $Ce(NO_3)_3.6H_2O$ (99.9% trace metals basis) were purchased from Sigma Aldrich. Dry ice was obtained from BOC Gases Ireland. All chemicals were used without further purification.

Instrumentation: X-ray diffraction patterns were recorded on a Bruker D2 benchtop diffractometer using Cu Kα radiation (λ = 1.5418 Å) across a 2θ range of 15 to 55° with a step–size of 0.01° at 1 s/step using a zero–background Si sample holder. Unit cell parameters and crystallite size were determined by Rietveld refinement of the obtained patterns performed using GSAS implemented in EXPGUI [34,35]. The starting point for refinements was (R -3c; a = 4.99; c = 17.0615) [36].

Scanning Electron Microscopy was carried out on a Zeiss Ultra Plus Scanning Electron Microscope operating at 3.00 kV.

Phosphorescence data was collected using a Horiba FluorMax-4 in phosphorimetry mode. Steady state measurements were made using a 0.1 ms delay, sample window of 25 ms and a flash count of 200 and an increment of 1 nm, using a solid-state powder. Excitation spectra were measured using excitation and emission slits of 2 nm and 2 nm while Emission spectra were measured using excitation and emission slits of 3 nm and 3 nm. Phosphorescence lifetime decay was determined using the decay by window mode, using an increment and max of, in addition it was carried out using a flash delay of 0.05 ms, a flash count of 200 and excitation/emission slits of 3 nm and 3 nm.

Inductively coupled plasma mass spectrometry (ICP-MS) was performed using an Agilent 7900 ICP-MS (G8403A) with an internal europium standard of europium oxide in 2% HNO_3 in combination with an internal indium standard.

Appendix A. Supplementary data

Supplementary material related to this article can be found, in the online version, at doi:https://doi.org/10.1016/j.mtcomm.2019.100590.

References

[1] F. Karakaş, et al., Prog. Org. Coat. 83 (2015) 64.
[2] S. Maleki Dizaj, et al., Expert Opin. Drug Deliv. 10 (2015) 1649 12.
[3] A. Som, et al., Nanoscale 25 (8) (2016) 12639.
[4] J.W. Morse, et al., Chem. Rev. 2 (107) (2007) 342.
[5] F.C. Meldrum, International Materials Reviews 3 48 (2003) 187.
[6] R. Chang, et al., Front. Energy Res. 17 (2017) 5.
[7] N.K. Dhami, et al., Front. Microbiol. 4 (2013) 314.
[8] M. Voigt, et al., Chem. Geol. 462 (2017) 30.
[9] L.Z. Lakshtanov, S.L.S. Stipp, Geochim. Cosmochim. Acta 4 (68) (2004) 819.
[10] N.L. Rosi, C.A. Mirkin, Chem. Rev. 4 (105) (2005) 1547.
[11] L. Wang, et al., Angew. Chemie Int. Ed. 37 (44) (2005) 6054.
[12] Y. Boyjoo, et al., J. Mater. Chem. A 35 (2) (2014) 14270.
[13] F.C. Donnelly, et al., Chem. Commun. 49 (53) (2017) 6657.
[14] R.D. Shannon, Acta Crystallographica Section A 5 (32) (1976) 751.
[15] B.R. Heywood, S. Mann, Langmuir 5 (8) (1992) 1492.
[16] D. Rautaray, et al., CrystEngComm 106 (4) (2002) 626.
[17] A.F. Wallace, et al., Science 6148 (341) (2013) 885.
[18] R. Wiebe, V.L. Gaddy, J. Am. Chem. Soc. 4 (62) (1940) 815.
[19] V. Blanco-Gutierrez, et al., J. Mater. Chem. C 46 (2) (2014) 9969.
[20] P.A. Tanner, Chem. Soc. Rev. 12 (42) (2013) 5090.

[21] G.J. Gao, et al., Opt. Express 23 (18) (2010) A575.
[22] Y.F. Wu, et al., J. Am. Ceram. Soc. 4 (95) (2012) 1360.
[23] Y.Z. Dai, et al., Crystengcomm 20 (19) (2017) 2758.
[24] Y. Gao, et al., Materi. Sci. Eng. B-Adv. Funct. Solid-State Mater. 203 (2016) 52.
[25] H. Li, et al., Powder Technol. 2 (212) (2011) 372.
[26] Y.D. Sun, et al., J. Mater. Chem. C 20 (3) (2015) 5316.
[27] M. Liu, et al., Appl. Phys. A 3 (124) (2018) 249.
[28] Y. Onishi, et al., J. Appl. Phys. 11 (55) (2016) 112401.
[29] M. Shang, et al., ACS Appl. Mater. Interfaces 7 (3) (2011) 2738.

[30] J. Nara, S. Adachi, Ecs J. Solid State Sci. Technol. 7 (2) (2013) R135.
[31] K. Sawada, et al., J. Alloys. Compd. 678 (2016) 448.
[32] Y. Onishi, et al., J. Appl. Phys. 11 (55) (2016) 6.
[33] Q. Cheng, et al., J. Lumin. 156 (2014) 91.
[34] A.C. Larson, R.B. Von Dreele, General structure analysis system (GSAS), Los Alamos National Laboratory Report LAUR 86–748 (1994).
[35] B.H. Toby, J. Appl. Crystallogr. 34 (2001) 210.
[36] D.L. Graf, Am. Mineral. 11–12 (46) (1961) 1283.